Fast simulated annealing and adaptive Monte Carlo sampling based parameter optimization for dense optical-flow deformable image registration of 4DCT lung anatomy

Tai H. Dou, Yugang Min, John Neylon, David Thomas, Patrick Kupelian, et al.

Tai H. Dou, Yugang Min, John Neylon, David Thomas, Patrick Kupelian, Anand P. Santhanam, "Fast simulated annealing and adaptive Monte Carlo sampling based parameter optimization for dense optical-flow deformable image registration of 4DCT lung anatomy," Proc. SPIE 9786, Medical Imaging 2016: Image-Guided Procedures, Robotic Interventions, and Modeling, 97860N (18 March 2016); doi: 10.1117/12.2217194

SPIE.

Event: SPIE Medical Imaging, 2016, San Diego, California, United States

Fast simulated annealing and adaptive Monte Carlo sampling based parameter optimization for dense optical-flow deformable image registration of 4DCT lung anatomy

Tai H. Dou, Yugang Min, John Neylon, David Thomas, Patrick Kupelian, and Anand P. Santhanam
Department of Radiation Oncology, University of California, Los Angeles, CA, USA

ABSTRACT

Deformable image registration (DIR) is an important step in radiotherapy treatment planning. An optimal input registration parameter set is critical to achieve the best registration performance with the specific algorithm. *Methods* In this paper, we investigated a parameter optimization strategy for Optical-flow based DIR of the 4DCT lung anatomy. A novel fast simulated annealing with adaptive Monte Carlo sampling algorithm (FSA-AMC) was investigated for solving the complex non-convex parameter optimization problem. The metric for registration error for a given parameter set was computed using landmark-based mean target registration error (mTRE) between a given volumetric image pair. To reduce the computational time in the parameter optimization process, a GPU based 3D dense optical-flow algorithm was employed for registering the lung volumes.
Numerical analyses on the parameter optimization for the DIR were performed using 4DCT datasets generated with breathing motion models and open-source 4DCT datasets.
Results showed that the proposed method efficiently estimated the optimum parameters for optical-flow and closely matched the best registration parameters obtained using an exhaustive parameter search method.

Keywords: non-rigid registration, 3D optical-flow, 4DCT, adaptive Monte Carlo, simulated annealing

1. INTRODUCTION

Deformable image registration (DIR) algorithms for lung anatomy aim to provide an accurate estimation of non-rigid volumetric deformations between a given pair of 3D lung images. DIR is an effective tool in lung radiotherapy's treatment planning, where reducing uncertainties in tumor motion during breathing allows for lung tumor dose escalation while sparing healthy lung tissue. With radiotherapy techniques such as the stereotactic body radiation therapy and proton therapy that are sensitive to the tumor motions, the accuracy of DIR becomes increasingly important [1, 2]. DIR is also a key step in developing individualized physiological breathing models from 4DCT images, which is an CT acquisition of lung anatomy gated at different breathing phases [3-5], and can aid in the development of model-guided dose simulations, dynamic ventilation simulation and online image guidance.

Lung DIRs has been previously investigated using a large number of algorithms [2, 6-10], of which optical-flow methods have proven to be effective [2, 9-11]. Dense optical-flow estimated motion based on a global balance between pixel intensity conservation and smoothness between successive frames [12]. The accuracy of the optical-flow image registration has been steadily improving in recent years [6, 13-15]. Guerrero *et al* demonstrated accurate lung tumor motion estimation using 3D optical-flow methods [16]. Samant *et al* introduced an implementation of a variant of the optical-flow, demons, on a GPU and opened the door to the application of adaptive radiation therapy with a near real-time DIR performance [17].

Computationally, given a registration algorithm with its associated transformation model and computation scheme, the parameter setting determines the registration accuracy. Recent work by Kashani *et al* showed that different parameter settings for the same type of registration led to variations in the DIR accuracy [18]. Moreover, Kadoya *et al* identified the lack of optimized parameters as a limitation for determining the optimum DIR algorithm accuracy [9]. Mathematically, the relationship between the registration parameters and the registration error is susceptible to

Medical Imaging 2016: Image-Guided Procedures, Robotic Interventions, and Modeling,
edited by Robert J. Webster III, Ziv R. Yaniv, Proc. of SPIE Vol. 9786, 97860N

local minima due to a non-convex nature of DIR formulation [19]. In the case of optical-flow DIR, the domain for the parameters (smoothness term, number of optical-flow resolutions, and solver iterations) is large. The proper choice of the registration parameters can result in greatly improved registration accuracy. The optimal smoothness value depends on the level of noise and artifacts in the 4DCT images, and may therefore change from one 4DCT case to another. Finding the optimal number of solver iteration enables one to obtain optimal registration accuracies. Moreover, in multi-resolution approaches, for a given image registration, there can be generally an optimal number of levels with its associated sets of smoothness factor and required solver iterations. Optimizing these parameters through trial-and-error can be very labor-intensive and error-prone. Recent studies reflect the necessity of a more systematic approach to explore this problem for 4DCT lung registration. In [14, 15], the authors fixed, among the registration parameters, the regularization weight for their algorithm performance evaluation. Rühaak *et al* investigated the target registration error (TRE) variation due to varying individual parameter sensitivity, with respect to a set of the 4 regularization weighting parameters [20]. By fixing three out of four parameters at one time and studying the change in TRE due to one parameter alone, their observed variation in TRE can be as large as 3 mm. In [7, 21], the authors determined the optimal regularization weight by averaging over a set of 5 and 10 data sets, respectively, and applied the averaged value to all cases. Schmidt-Richberg *et al* investigated single parameter optimization for a specific optical-flow implementation and showed an initial feasibility of improvement in registration accuracy on a case-by-case basis [22]. A systematic approach to optimal parameter selection is however desirable if the registration involves several input parameters. To the best of our knowledge, a multi-parameter optimization framework for deformable image registration in the thorax has not been previously investigated. Thus, our aim is to analyze the optimal registration parameter combination and their effect on the registration accuracy.

Various approaches have been applied to find the optimal algorithm parameters, such as the discrepancy principle [23-25], generalized cross validation [26, 27] and the L-curve based method [28, 29]. Their common disadvantage is the high computational cost, which is undesirable especially in large-scale problems. In the case of discrepancy principle, prior information on the noise level or a bound on the signal is required. As for the generalized cross validation, the computation of the singular value decomposition of the system matrix is required in an efficient implementation of the Tikhonov regularization, which is very computationally demanding in large scale problems [30]. With respect to the L-curve approach, it may be necessary to solve least squares problem for several parameters and is also known to suffer from its asymptotic behavior as the size of the parameters increases [31]. This paper proposes a multi-parameter strategy for estimating the optimal registration parameters that lead to the minimization of registration errors for a given registration method. Specifically, we employ a technique that will be able to address the undesired local minima problem for the DIR objective function, which represents the generalized evaluation of the dissimilarity between the deformed volume and the target volume. The parameter domain is sampled using a fast-simulated annealing scheme with adaptive Monte Carlo (FSA-AMC) sampling approach. To account for a multi-local minima problem, the proposed iterative technique, while searching for an increasingly better parameter set, also adaptively includes a random parameter set. Thus, this technique effectively reduces the possibility of solutions being trapped in a local minimum during parameter optimization. In this paper, we investigate the application of a Fast Simulated Annealing with Adaptive Monte Carlo sampling (FSA-AMC) algorithm as a global optimizer over the combinatorial multi-parameter domain of the underlying dense optical-flow registration algorithm. The registration improvements are presented that show our proposed method accurately estimates the optimal Optical-flow DIR parameters for each of the given 4DCT exhale-inhale volume pairs. The paper is organized as follows: The theoretical framework that underlies the image registration and the proposed FSA-AMC algorithm is described in Section II. In Section III, the results obtained by applying the proposed technique to 4DCT lung image data are presented. Finally, we conclude and discuss future outlook in Section IV.

2. METHODS

The overall parameter optimization process was structured as three nested loops. The inner-most loop was the multi-resolution dense optical-flow algorithm [12] that for a given registration parameter set evaluated a cost value. The outer two loops involved the FSA-AMC parameter optimization process that estimated a candidate parameter set based on the cost values evaluated in the previous two FSA-AMC iterations, and FSA-AMC's control parameter.

2.1 Inner most loop: multi-resolution optical-flow method

The multi-resolution dense optical flow algorithm has been investigated by peers [12]. For clarity purposes, we briefly explain the registration process. Let $f: \Omega_R \rightarrow R$ denote the fixed static image and $g: \Omega_R \rightarrow R$ the moving template image, with $\Omega \in R^3$ denoting the image domain. In image registration, a transformation $v: R^3 \rightarrow R^3$ was to be solved, such that the fixed static image f and the deformed template image g_v are similar. Mathematically, image registration was formulated as minimizing energy functional with respect to a deformation field v. The energy consisted of two terms:

$$\mathcal{J}(\vec{v}) = \underbrace{\int_{\Omega_R} \mathcal{D}(v)}_{data\ term} + \underbrace{\alpha \int_{\Omega_R} R(v)}_{regularization\ term} . \tag{1}$$

For the Horn-Schunck optical-flow [12-16], the formulation becomes

$$\mathcal{J}(\vec{v}) = \int_{\Omega_R} (\nabla I \cdot v + I_t)^2 + \alpha \int_{\Omega_R} \sum_{x=1}^{3} \| \nabla v_x \|^2 \, dx, \tag{2}$$

where the first term represented the optical-flow gradient constraint, the second term was the regularization term, with α as the weighting factor for the smoothness constraint. The gradient constraint was based on the central optical-flow assumption that local intensities of a motion sequence between the two images f and g are conserved. The regularization term was introduced to alleviate the ill-posedness of the problem by enforcing smoothness of the deformation field, v. The problem was solved using calculus of variations. Optical-flow vector field was obtained by applying iterative Gauss-Seidel method that solve the Euler-Lagrange equations:

$$v_{x,j}^{k+1} = \bar{v}_{x,j}^{k} - \frac{I_{x,j}\left(I_{x,j}\bar{v}_{x,j}^{k} + I_{y,j}\bar{v}_{y,j}^{k} + I_{z,j}\bar{v}_{z,j}^{k} + I_{t,j}^{k}\right)}{\alpha^2 + I_{x,j}^2 + I_{y,j}^2 + I_{z,j}^2} \tag{3.a}$$

$$v_{y,j}^{k+1} = \bar{v}_{y,j}^{k} - \frac{I_{x,j}(I_{x,j}\bar{v}_{x,j}^{k} + I_{y,j}\bar{v}_{y,j}^{k} + I_{z,j}\bar{v}_{z,j}^{k} + I_{t,j}^{k})}{\alpha^2 + I_{x,j}^2 + I_{y,j}^2 + I_{z,j}^2} \tag{3.b}$$

$$v_{z,j}^{k+1} = \bar{v}_{z,j}^{k} - \frac{I_{x,j}(I_{x,j}\bar{v}_{x,j}^{k} + I_{y,j}\bar{v}_{y,j}^{k} + I_{z,j}\bar{v}_{z,j}^{k} + I_{t,j}^{k})}{\alpha^2 + I_{x,j}^2 + I_{y,j}^2 + I_{z,j}^2} \tag{3.c}$$

with smoothness factor $\alpha \in [\alpha_{min}, \alpha_{max}]$, iteration index $k \in [1, k_{max}]$, and level index $j \in [1, j_{max}]$. To account for the large voxel displacements due to respiratory motion, multi-resolution approaches were commonly adopted. Down-sampling was performed in all dimensions, which included a Gaussian smoothing and reduction in all dimensions by the selected down-sampling factor. The lowest resolution level images were first registered. The resulting deformation vector-field were taken as initial condition for the next level of higher resolution. In this manner, the details in the higher resolution levels were progressively refined.

2.2 Outer loops: FSA-AMC

Let $S = (s_1, s_2, \ldots, s_n)$ be a solution candidate in the *n*-dimensional solution space of the transformation for volumetric alignment, where s_i is the i^{th} parameter of the transformation model, with (s_i^{min}, s_i^{max}) defining the domain of each parameter. In this global coarse-to-fine scheme, we identified the three pertinent parameters: the smoothness factor, s_1, the iteration number, s_2, and the number of levels, s_3. For registering two images, f and g, an objective function *O* that evaluates the dissimilarity between these two images can be defined as follows:

$$O = O\big(f\big(S(x)\big), g(x)\big), \tag{4}$$

where *x* denotes a voxel in the image space and *O* can be multimodal and non-smooth. The most suitable geometrical transformation between a pair of images was estimated by determining the optimal set of these parameters. Thus, the optimal transformation *S* that brings f into alignment with g can be formulated as an optimization problem

$$\hat{S} = \underset{S \in \{S_1, \ \ldots, \ S_n\}}{\arg min} [O(f(S(x)), g(x))]. \tag{5}$$

The aim of the FSA-AMC was to find a feasible solution from the joint multi-parameter domain that minimized the objective function. FSA algorithm [32, 33] consists of three components: (a) solution candidates generation from a probability distribution that allowed for parameter space sampling; (b) an acceptance criterion that determined according to the acceptance probability whether a hill-climbing step should take place; and (c) an annealing schedule that employed an artificial cooling temperature as a control parameter. FSA distinguished itself from the classical simulated annealing in that FSA included occasional long jumps in the parameter domain and allowed for more efficient local minima verification, in contrast to the strictly local search approach in classical simulated annealing, [33]. The proposed optimization scheme using FSA-AMC can be described as follows. The initial sampling density ρ^0 was defined as

$$\rho^0(s_i) = \frac{1}{s_i^{max} - s_i^{min}}, \ s_i^{min} < s_i < s_i^{max}. \tag{6}$$

A set of solution candidates $\{S_1^0, S_2^0, S_i^0, \ldots \ S_N^0\}$ was generated using the initial sampling density ρ^0. Each of the solution candidates S_i was evaluated for its objective function. The two candidates that rendered the smallest objective function (4) values were stored as the starting points for the FSA-AMC process (S^1 and S^2) with S^2 being the smallest objective function. The control parameter in FSA, T_K, decreased in the course of the optimization process and was defined as

$$T_K = \frac{T_o}{K}, \tag{7}$$

where *K* was the iteration index.

To allow for a thorough local parameter space sampling, a two-layered FSA optimization was employed. The outer loop generated the candidate solution based on optimization from the immediate preceding iteration at each annealing temperature. The inner loop, on the other hand, involved a number of m_{max} iterations to ensure the local parameter space is searched sufficiently at a given temperature. At the K^{th} FSA temperature and m^{th} inner loop, the sampling density for each of the parameters was based on a Cauchy distribution and defined as

$$\rho^{K,m}(s_i) = \frac{1}{\pi\sigma_i(\Delta O_{K,m}/\Delta O_3)\left[1+\left(\frac{s_i - \hat{s}_i^{K-1,m}}{\sigma_i(\Delta O_{K,m}/\Delta O_3)}\right)^2\right]} \tag{8}$$

where σ_i is the base standard deviation of ρ^K for s_i and is expressed as

$$\sigma_i = \frac{s_i^{max} - s_i^{min}}{4} \tag{9}$$

the term $\sigma_i(\Delta O_{K,m}/\Delta O_{0,3})$ modified the width of the sampling density with the derived cost gradients $\Delta O_{0,3}$ and $\Delta O_{K,m}$, from the starting cost values and the subsequent nested iterations, defined as:

$$\Delta O_{0,3} = O(S^{0,2}) - O(\hat{S}^{0,1}) \tag{10.a}$$

$$\Delta O_{K,m} = O(S^{K,m}) - O(\hat{S}^{K,m-1}) \tag{10.b}$$

and finally, $\hat{S}^{K,m-1}$ was the accepted parameter candidate for a given annealing temperature *K*. The parameter set $S^{K,m}$ was randomly generated by analytic inversion method for (7) using

$$s_i = \sigma_i \left(\frac{\Delta O_{K,m}}{\Delta O_3}\right) \cdot \tan\left[\left(\mu - \frac{1}{2}\right)\pi\right] + \hat{s}_i^{K,\mathrm{m}-1} \tag{11}$$

where μ was sampled between (0, 1).

At each iteration, the parameter selection was determined using the acceptance probability $p^{K,m}{}_A$ according to the Metropolis criterion [34]:

$$p^{K,m}{}_A = \min\left\{1, \exp\left(-\frac{\Delta O_{K,m}}{T_K}\right)\right\} \tag{12}$$

where the Boltzmann weight $\exp\left(-\frac{\Delta O_{K,m}}{T_K}\right)$ was computed using T_K and ΔO values from (6) and (9), respectively. If $\Delta O \leq 0$, the new parameter set was accepted as the new center for estimation. On the other hand, if $\Delta O > 0$, the value of $p^{K,m}{}_A$ was compared with a random probability p_r, ranging between 0 and 1. The criterion for accepting $\hat{S}^{K,m}$ as the candidate solution for the next iteration was $p^{K,m}{}_A > p_r$. If unsatisfied, the candidate solution for the next iteration in the inner loop of $\hat{S}^{K,m}$ remained the same as $\hat{S}^{K,m-1}$. To prevent the loss of good solutions, in each of the inner iterations, the cost value of the sampled candidate solution, $S^{K,m}$, was compared to that of the previous minimum solution S_{min} and updated as the new S_{min} if $S^{K,m} < S_{min}$. When the inner loop reached near equilibrium, the final parameter set was passed onto the outer loop. The above process was repeated to find the optimal solution candidate for each annealing temperature. The whole optimization process ended when the outer loop reached a sufficiently low temperature.

The adaptive nature of the sampling distribution is evident in equation (8), where the center and width of the Cauchy distribution is refined during each optimization step. The use of Cauchy distribution preserved the locality of the previously accepted candidate solution, but the presence of a small number of very long jumps in the parameter domain allowed for faster escape from local minima as well as more efficient sampling of the parameter space. Equation (12) allows for the acceptance of solutions that do not decrease the cost values by hopping between the local minima in the beginning of the optimization process. As the iteration number increases, the parameter T_k becomes small, which in turn causes the acceptance probability to become small, solutions that do not decrease the cost gradient become increasingly unlikely to be accepted as the candidate solution.

3 IMPLEMENTATION

The proposed method is schematically represented in Fig. 1 and can be described as follows. As explained in Section II.A, a total of 3 parameters were selected; with the lower and upper bounds for the s_1 smoothness factor and s_2 solver iteration defined as the following :(s_1^{min}, s_1^{max}, s_2^{min}, s_2^{max}) = (0, 800, 0, 700). Smoothness factors larger than 800 were found not to contribute to the registration accuracy, and iteration of 700 were verified to fulfill numerical convergence in the studied cases. The range of values for the downscale sampling rate was s_3 = (1.1, …, 2.5) in increments of 0.1. Accordingly, the resulting number of resolution levels that can be obtained by varying degree of sample rate ranges from 3 to about 30, depending on the specific image data dimensions. Down-sampling values greater than 2.5 were found not to contribute to the improvement of accuracy. The first step involved selecting a pair of starting solution candidates. For this purpose, we randomly selected a set of 20 registration parameters. The initial estimate of the cost gradients and the value (computed using equation (4)) were derived from the two best solutions that render the least cost values among this initial set. Then, in the optimization process, a total of K_{max} iterations were performed. The starting annealing temperature was set to 5 so that, accounting for the iterations it takes for the acceptance probability (eq. 12) to become negligible, the whole optimization can be completed in acceptable computation times. In each iteration, the new solution candidate was selected based on the adaptive Monte Carlo sampling as in (7). The goodness of the solution candidate was evaluated using the objective function cost value (equation (4)) for known ground truth deformation. The previous best-cost value was compared against the current cost value and was updated whenever applicable. Whether the current solution candidate was accepted as the sampling point was determined by the

Metropolis criterion. The annealing schedule was designed so that the Boltzmann weight diminishes in the course of the optimization process.

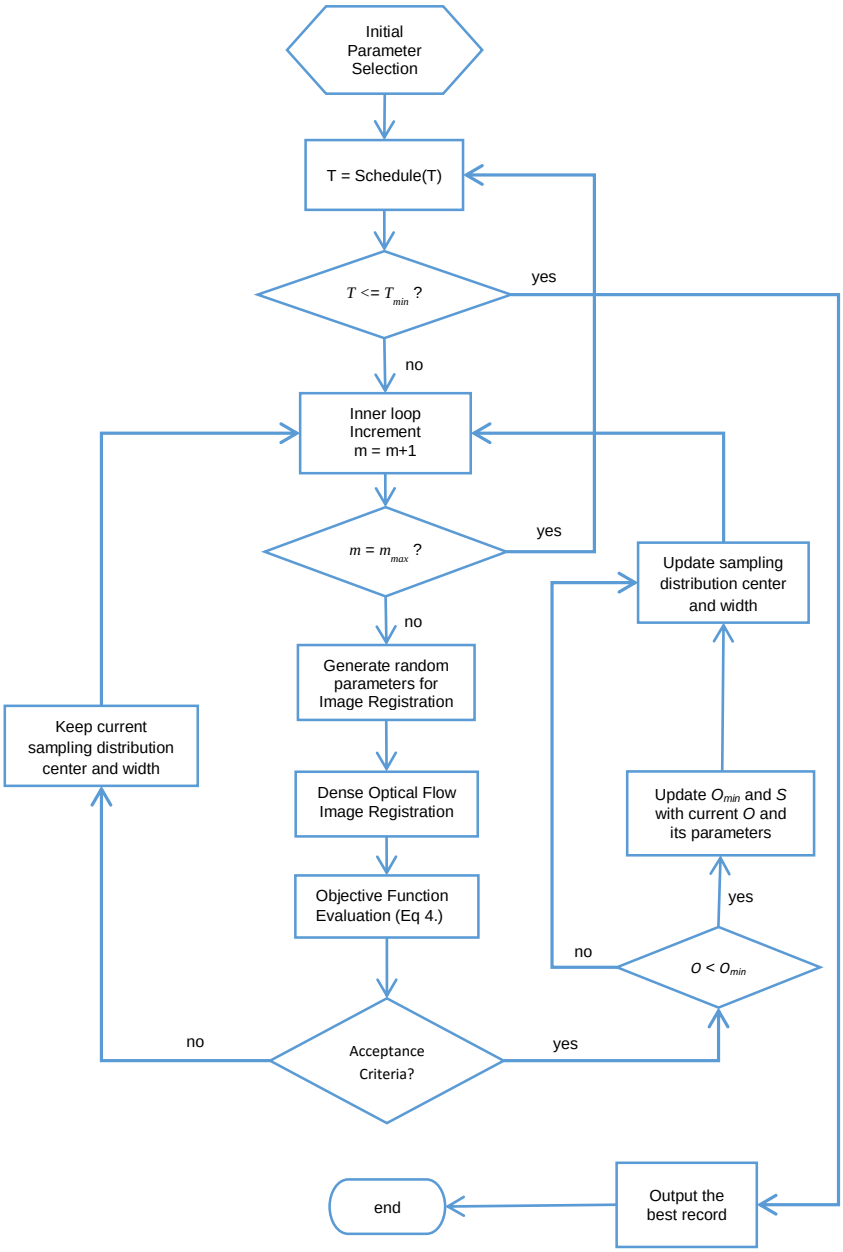

Figure 1. Overview of the FSA-AMC parameter optimization for registration algorithm. The flowchart displays the individual steps performed in the optimization process, as described in Section II-B.

4 EXPERIMENTS

4.1 Input Data

The model-guided 4DCT eliminated image artifacts that may occur in commercial 4DCT acquisition system due to subject irregular breathing and improved the image SNR ratio [4, 35]. Key features of the breathing motion model were its noise-reduced and artifacts-reduced images available at any user-selected breathing phase during the breathing cycle. The accuracy of the model generated image has been reported in [35]. The model provided 3D lung images with anatomically accurate Hounsfield units at different breathing phases, which is critical to test the robustness of our proposed method. The dimensions of the model guided 4DCT data were 300×200×230 with voxel size of 1 mm ×1 mm × 1mm. The images were cropped to include the rib cage for conventional whole lung registration.

Registration accuracy was evaluated based on landmark features identified in the source and target images. For our analysis, the lung anatomy at 15 percent breathing phase in a given 4DCT was taken as the static or reference 3D image as it represented the lung anatomy close to the end-exhalation breathing phase. Similarly, the lung anatomy at 85 percent breathing phase in a given 4DCT was taken as the moving or deformed 3D image as it represented the lung anatomy close to the end-inhalation breathing phase. To select large number of landmark features as ground truth for registration accuracy evaluation, over 1000 uniformly distributed landmark pairs in the intensity range of -600 HU to 100 HU for each lung were initially selected from an arbitrary reference phase (see Fig. 2). The usage of such a large number of landmarks provided a global measurement on the spatial accuracy over nearly the entire lung tissue voxels. The coordinates of the selected

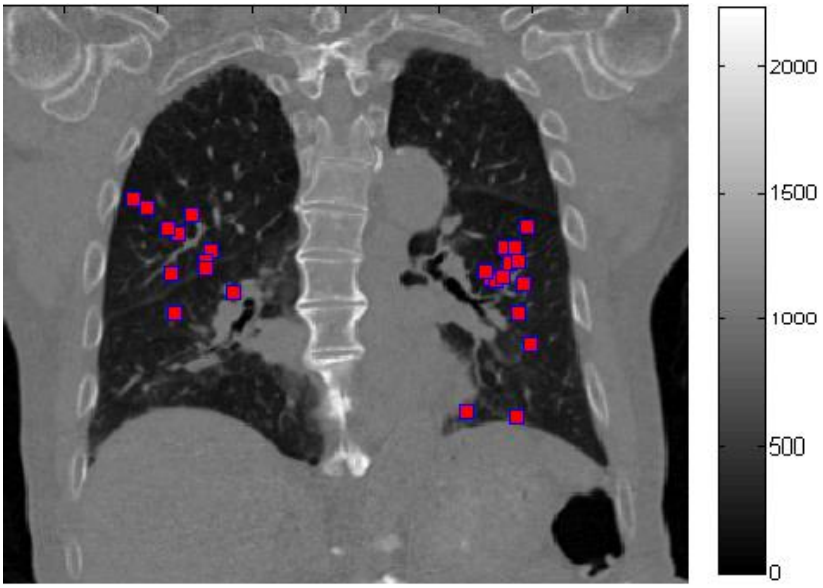

Figure 2. An example coronal image at 85 percentile breathing phase obtained for patient 1 of the breathing model data showing landmarks generated using the intensity criteria (see text).

points were then mapped to the 15-percent breathing phase (closer to end-exhalation phase) and 85-percent breathing phase (closer to end-inhalation phase) using model generated deformation vector fields. The resulting set of corresponding points between the 15 and 85 percent breathing phases were spatially distributed throughout each of the lungs, with the number of features pairs per lung ranging from 1042 to 1484.

The mean and standard deviation of the ground truth displacement are listed in Table 1 and are quantified as the Euclidean distance between the target voxels in the 85 percent breathing phase images and the corresponding source voxels in the 15 percent breathing phase images. The average landmark displacement per lung ranges from 3.36 to 7.76 mm (see Table 1).

To further test our method with real data sets, the data provided by the "University of Texas M.D. Anderson Cancer Center" was also used. 4DCT scan of the thorax and abdomen was obtained from patients treated for esophageal or lung cancer. Image data had a slice thickness of 2.5 mm, with in-plane resolution ranging from 0.97 to 1.16 mm. This publicly available data set (www.dir-lab.com) also included ground truth in terms of landmark coordinates that can be used to validate the accuracy of motion flow calculations. A total of 5 cases were examined, using the 300 annotated landmark points provided per case. These landmarks were uniformly distributed throughout the lungs and have been selected with an intra-observer of ~1mm. On average, the maximum displacement for these 5 cases was over 15 mm [6]. The mean and standard deviation of the truth displacement are listed in Table 3.

The objective function in equation (4) was employed to compute the registration accuracy using the landmark displacements. In this case, the *f* and *g* images were considered to be the warped source images using the displacement computed using the DIR and the landmark displacement, respectively.

4.2 FSA-AMC Optimization

In our experiment, we performed two variations of FSA-AMC optimization. In the first variant, we performed a two-parameter optimization on the combined parameter set of the smoothness factor and solver iterations. For this experiment, the down-sampling factor was fixed at 2, as is commonly done. On the other hand, a three-parameter FSA-AMC optimization was performed by including the down-sampling factor as the third parameter. Studies of combinatorial parameter optimization were performed on the 5D breathing model data as well as on the DIR-LAB cases. To explore the possibility of registration accuracy improvement from single lung registrations using each of the variants, the left and right lungs were cropped and their optimal registration parameters are estimated. These results were also compared to the whole lung registrations. Validation studies using an exhaustive search approach were conducted to compare with the FSA-AMC results. A large number of registrations were performed using input parameters over the entire parameter domain sampled regular interval grids. The grids were in units of 20 smoothness values and 20 solver iterations, with the full 15 down-sampling factors. For validating 2 parameter FSA-AMC optimizations, a total of 1400 individual registrations were performed for each source-target pair. On the other hand, the validation for 3 parameter optimizations was performed by including a set of 15 down sampling factors.

5 RESULTS

In this section, we present the results of FSA-AMC optimization as well as the validation studies. Fig. 3 shows an example output on the coronal cross section. The moving image (Fig. 3(a)) is deforming to the static image (Fig. 3(b)) to produce an *ad hoc* deformed image (Fig. 3(c)) and an optimally deformed image (Fig. 3(d)). The effect on the registered images due to parameter optimization can be appreciated qualitatively by observing the difference image between the original images (Fig. 3(e)), difference image between static and deformed image using an arbitrary registration parameters (Fig. 3(g)), and difference image between static and deformed image using the optimal registration parameters (Fig. 3(h)). The vector flow field attained through the optimal image registration is illustrated in (Fig. 3(f)).

Comparison with the mean displacements of the selected landmarks (Table 1 vs Table 2 and Table 3 vs Table 4) shows quantitatively that the registration accuracy gain due to FSA-AMC. The registration results from both datasets show that the obtained mTRE, computed from equation (4) for known ground truth deformation, is below the limiting slice thickness or approaches it (1 mm for the breathing model data and 2.5 mm for open source data).

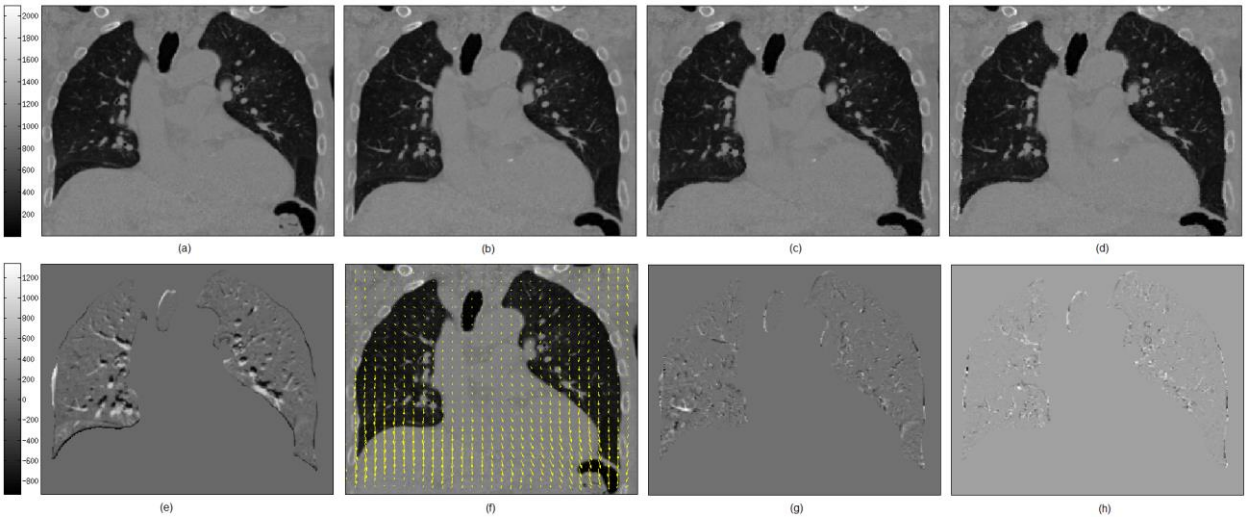

Figure 3**.** Images of a sample coronal cross section obtained for patient 1 of the breathing model: (a) exhale (moving) image, (b) inhale (static) image, (c) deformed exhale image obtained using arbitrary registration parameters, (d) deformed exhale image obtained using the optimal registration parameters, (e) difference between static and moving images, (f) displacement vectors overlaid on the moving images, (g) difference between static and deformed moving image using an arbitray registration parameter set, (h) difference between static and deformed moving image using optimal registration parameters.

Table 1. Breathing model generated 4DCT data description

	Patient 1 (left)	Patient 1 (right)	Patient 1 (whole)	Patient 2 (left)	Patient 2 (right)	Patient 2 (whole)
Average Displacement (mm) (SD)	8.295 (4.76)	13.76 (7.76)	11.10 (7.03)	9.48 (5.38)	6.69 (3.36)	8.22 (4.79)
Landmark size	1409	1484	2893	1259	1042	2301

Table 2. Registration Results of FSA-AMC 3D optical-flow calculation on breathing model generated 4DCT data

Data	Optimization	Lung registered	Smoothness factor	Solver Iteration	Down-sampling factor	$\begin{pmatrix} Resolution \\ Levels \end{pmatrix}$	Cost Value (mm)	Combined cost value (mm)
Patient 1	2 parameter	left	10.18	162	2	8	0.811± 1.636	
	2 parameter	right	10.06	243	2	8	1.089 ± 1.997	0.953± 1.830
Patient 1	3 parameter	left	15.25	481	2.1	6	1.162 ± 2.477	
	3 parameter	right	15.14	462	1.3	16	0.460 ± 0.231	0.802 ± 1.737
Patient 1	2 parameter	whole	10.11	425	2	8	-	0.783 ± 1.508
	3 parameter	whole	43.86	384	1.3	17	-	**0.436 ± 0.251**
Patient 1	*ad hoc*	Whole	400	400	2	8	-	3.359 ± 4.477
Patient 2	2 parameter	left	97.78	640	2	7	2.205 ± 3.488	
	2 parameter	right	244.90	481	2	8	0.478 ± 0.214	1.423 ± 2.584
Patient 2	3 parameter	left	93.25	218	2	7	2.204 ± 3.468	
	3 parameter	right	260.89	622	2.1	7	0.449 ± 0.200	**1.409± 2.569**
Patient 2	2 parameter	whole	107.02	617	2	8	-	1.446 ± 2.641
	3 parameter	whole	107.00	546	2	8	-	1.446 ± 2.641
Patient 2	*ad hoc*	Whole	400	400	2	8	-	2.422 ± 3.944

Table 3. MD Anderson 4DCT data description

	Case 1	Case 2	Case 3	Case 4	Case 5
Average Displacement (mm) (SD)	4.01 (2.91)	4.65 (4.09)	6.73 (4.21)	9.42 (4.81)	7.10 (5.14)
Maximum Displacement (mm)	12.65	17.8	18.46	21.0	24.78

Table 4. Registration results on FSA-AMC 3D optical-flow calculation on MD Anderson 4DCT data

Data	Optimization	Lung registered	Smoothness factor	Solver Iteration	Down-sampling factor	$(Resolution\ Levels$	Cost Value (mm)	Combined cost value (mm)
case 1	2 parameter	left	204.748	573	2	7	1.386 ± 0.825	1.250 ± 0.759
	2 parameter	right	312.467	649	2	7	1.11 ± 0.683	
case 1	3 parameter	left	188.146	528	2.5	5	1.385 ± 0.873	1.249 ± 0.756
	3 parameter	right	208.998	586	2.5	5	1.107 ± 0.611	
case 1	2 parameter	whole	245.137	417	2	7	–	1.184 ± 0.630
	3 parameter	whole	244.775	540	2	7	–	**1.183 ± 0.630**
case 2	2 parameter	left	121.888	303	2	7	1.301± 0.798	1.296 ± 0.701
	2 parameter	right	138.14	623	2	7	1.292 ± 0.603	
case 2	3 parameter	left	147.193	687	2	7	1.306± 0.853	1.301 ± 0.730
	3 parameter	right	138.274	531	2	7	1.296 ± 0.603	
case 2	2 parameter	whole	142.221	450	2	7	–	**1.278 ± 0.686**
	3 parameter	whole	149.557	384	2	7	–	1.285 ± 0.704
case 3	2 parameter	left	74.775	330	2	7	2.000 ± 1.335	2.078 ± 1.342
	2 parameter	right	93.561	419	2	7	2.082 ± 1.348	
case 3	3 parameter	left	133.716	273	1.1	28	1.786 ± 1.085	1.939 ± 1.227
	3 parameter	right	92.17	419	2	7	2.081± 1.345	
case 3	2 parameter	whole	106.69	304	2	7	–	**1.903 ± 1.188**
	3 parameter	whole	108.906	298	2	7	–	1.914 ± 1.204
case 4	2 parameter	left	220.262	622	2	7	2.450± 2.046	2.667 ± 2.190
	2 parameter	right	231.619	318	2	7	2.827 ± 2.287	
case 4	3 parameter	left	226.624	468	2	7	2.461± 2.058	2.674 ± 2.193
	3 parameter	right	231.225	436	2	7	2.827 ± 2.285	
case 4	2 parameter	whole	264.91	508	2	7	–	**2.642 ± 2.116**
	3 parameter	whole	269.229	608	2	7	–	2.652 ± 2.124
case 5	2 parameter	left	65.813	401	2	7	1.889 ± 1.210	2.747 ± 2.202
	2 parameter	right	84.63	319	2	7	3.449 ± 2.760	
case 5	3 parameter	left	78.772	441	1.6	9	1.864 ± 1.257	2.566 ± 1.968
	3 parameter	right	55.11	151	1.6	9	3.116 ± 2.398	
case 5	2 parameter	whole	75.4863	565	2	7	–	2.723 ± 2.415
	3 parameter	whole	63.552	239	1.1	30	–	**2.536 ± 2.052**

The optimal parameters and the associated best registration errors on 5D breathing model guided data and the DIR-LAB 4DCT are listed in Table 2 and Table 4, respectively. The number of resolution levels corresponding to the down-sampling factor is listed in the next column. Upon inspection of both data sets together, across all cases of full lung registration, the optimal parameter combinations of smoothness factor, solver iteration, and down-sampling factor demonstrated a wide range of variation. Moreover, a strong variation in the optimal parameters was also observed from one dataset to another when considering both single-single (left vs. right) lung optimal deformations and single (left/right cropped) versus whole lung registrations. Larger smoothness factor corresponds to a smoother deformation.

While the optimal smoothness factor did not vary much for breathing model patient 1, a marked variation in this parameter was observed for all other examined cases, for both single and whole lung registrations. The optimal smoothness factor varied from as low as 10 to 312.467. The rather low optimal smoothness factor of 10 was however found only in breathing model patient 1. In terms of the optimal solver iterations, the optimal values varied widely in a range between 151 and 649. This points to a rather *weak correlation* between the optimal TRE and the number of required solver iteration. This can be explained by the observation that when further iteration is performed beyond the threshold value, the difference in TRE is numerically negligible. Thus, in 2-parameter and 3-parameter optimizations, if the obtained smoothness factor and the down-sampling factor were similar, there can be considerable difference in the optimal number of solver iteration. As for the down-sampling factor, while the conventional value of 2 was most often found in the parametric optimizations, values other than 2 were also estimated to be optimal. While down-sampling factors of less than 2 facilitates smoother upsampling between neighboring pyramid levels, smaller factor does not always contribute to the reduction of registration error. This observation suggested that parameter optimization should be performed for each given image pair to determine the down-sampling factor that leads to the greatest accuracy.

In the 7 examined cases, a trend was observed between the parametric optimizations with respect to the optimal factors for smoothness and down-sampling. When optimal down-sampling factor was the same in both 2-parameter and 3-parameter optimizations, the optimal smoothness factors were also similar. For the rest of the scenarios, the optimal smoothness factors showed a deviation (e.g. model patient 1 in Table 2 and case5 in Table 4). In the former case, the observation served as a self-verification between the two independent parametric optimizations, indicating a convergence to the optimum smoothness factor. The latter observation, however, was a direct evidence for the existence of multiple local minima in the underlying multi-parameter cost function surface. The examined cases showed clearly that an optimal down-sampling factor contributed to the reduction of registration errors, and the registration error reduction can be as much as 0.35 mm as seen in the case of patient 1.

In addition to the observed variation among the studied cases, comparison is also made on the mTRE results between FSA-AMC optimized parameter set and an *ad hoc* parameter set, which comprises of the median values of the smoothness factor and the solver iteration together with conventionally employed down-sampling factor of 2 (see Fig. 4). Across the 5 cases, the difference in mTRE showed a considerable variation, with an average of 0.39 mm and a maximum of 0.90 mm. In the case of the 2 model guided 4DCT datasets, a higher difference in registration error between FSA-AMC approach and an *ad hoc* parameter set was observed (Table 2), for patient 2 being *1* mm and for patient 1 amounting to *2.92* mm. These results strongly support the need for parameter optimization on a per case basis.

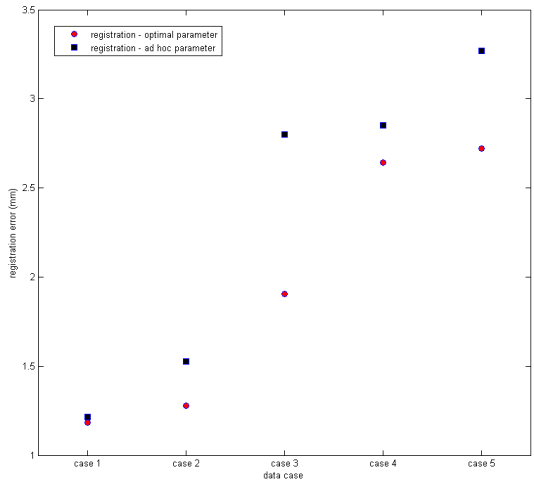

Figure 4. Comparison in whole lung registration errors for 5 DIR-LAB cases obtained using FSA-AMC optimized registration parameter set and an *ad hoc* one.

5.1 Validation Study

To validate the results obtained from 2-parameter as well as 3-parameter FSA-AMC optimization, exhaustive search was conducted by performing registrations over the entire parameter domain in regular interval grids. The grids are in units of 20 smoothness values and 20 solver iterations, with the full 15 down-sampling factors. This translates to 1400 grid points in the case of 2 parameter optimization. For a visualization of the underlying varied cost functions case-by-case, the surface plots of the cost functions in dependence of dense optical flow DIR smoothness and solver iteration parameters are displayed in Fig. 5 (a-g). The variations in the objective function's cost value for variations in the registration parameters is demonstrated. For an optimal smoothness parameter, the variations in the cost value for variations in the number of iterations varied from 0.3 mm – 0.7 mm. For worst case smoothness parameters, the variations in the cost value for variations in the number of iterations aried from 1 mm – 5 mm. The validation for 3 parameter was performed by computing cost value using smoothness factor and down-sampling factor, while the number of solver iteration is kept at a high number (~ 600) so that convergence with respect to this parameter was guaranteed.

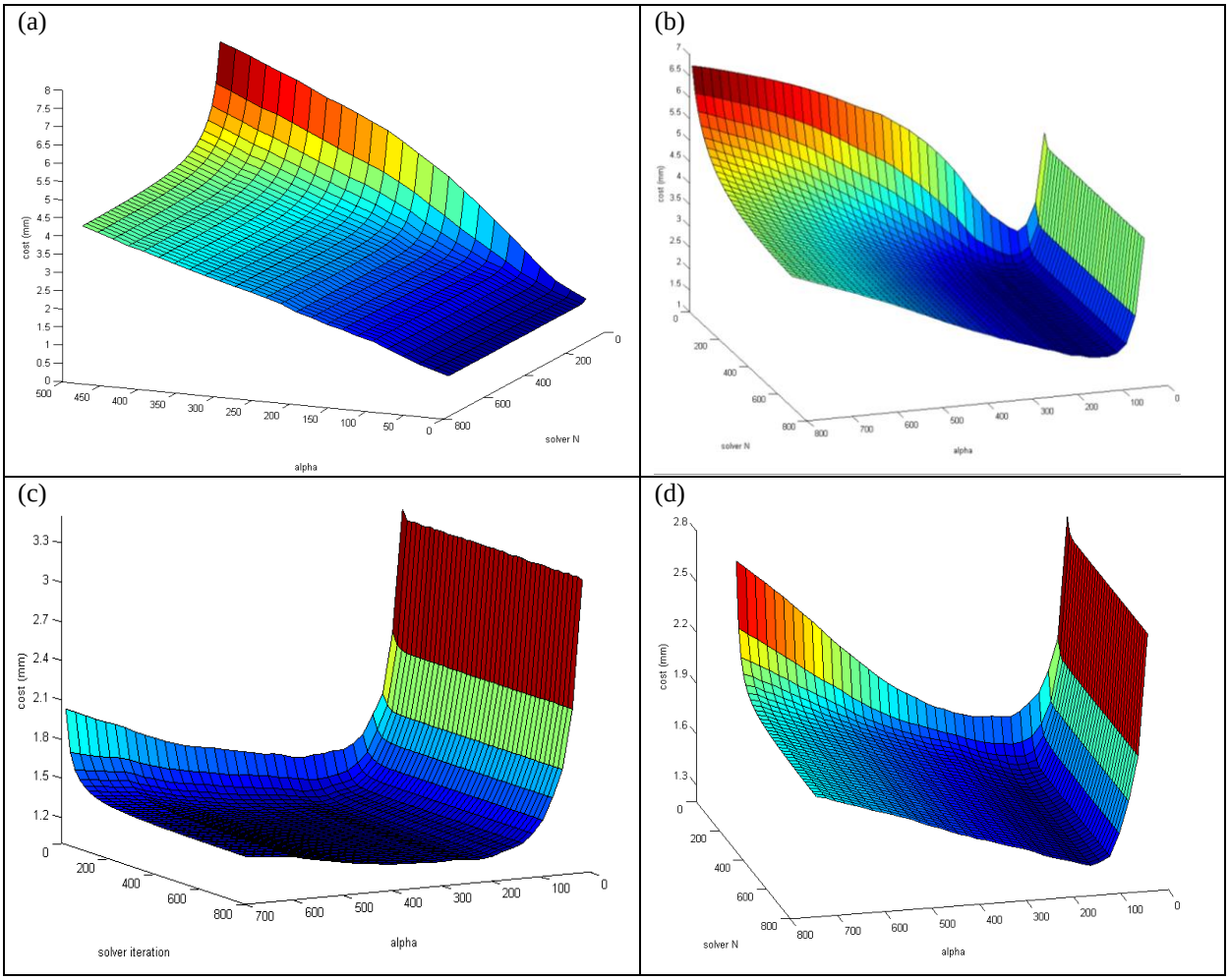

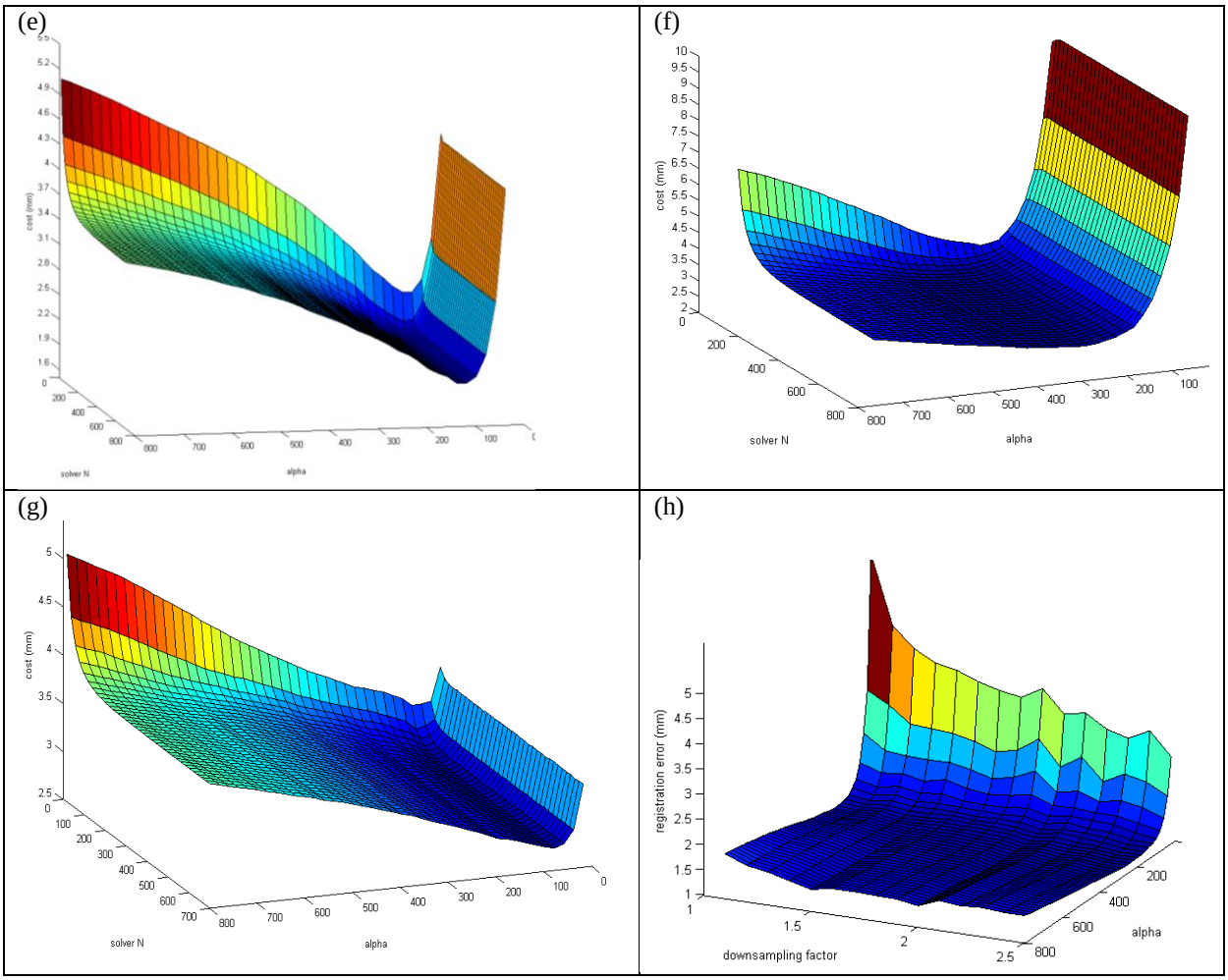

Figure 5. The objective function surfaces of registration errors using the given landmark points in dependence of the smoothness factor and the number of solver iteration for the breathing model data: a. patient 1, b. patient 2; and for the MD Anderson 4D CT data: c. case 1, d. case 2, e. case 3, f. case 4, g. case 5. h. The objective function surface for MD Anderson case 1 data in dependence of the smoothness factor and the down sampling factor. The presence of multiple regions of cost function minima is clearly visible.

In Fig. 5 (h), the complex surface with troughs of multiple cost function minima is shown as an example for DIR-LAB case 1. The optimal registration results obtained from the exhaustive search, as listed in Table 5a and 5b, respectively, were used for determining the accuracy of the FSA-AMC parameter optimization. Since the cost function varies in different degrees and sensitivity with respect to each parameter, a direct comparison on the values of the optimal parameters is not a good measure. To examine the results between the two methods, a Wilcoxon signed rank test was employed to test the hypothesis of zero mean for the paired differences in the obtained minimum mTRE for the 5 DIR-LAB cases. The resulting p-values for the 2-parameter and 3-parameter optimization were, respectively, 0.068 and 0.282. This indicates that the optimal parameters computed using the proposed method was in close agreement with the parameters obtained using the exhaustive search.

Comparative analysis of the single versus whole lung registrations showed that comparable mTRE between the two approaches. In fact, in all but one (see Table 4, case 3, 2 parameter optimization), the difference in mTRE was only numerical and less than 0.1 mm. This was also confirmed by Wilcoxon signed rank test, which showed that the mTRE difference was statistically insignificant.

Table 5a. Minimum Registration Error Using Exhaustive Search for Validating 2 Parameter Optimization

2	Left (mm)	Right (mm)	Whole (mm)
Case 1	1.386 ± 0.046	1.108 ± 0.037	1.176± 0.004
Case 2	1.304 ± 0.017	1.299 ± 0.005	1.286± 0.009
Case 3	2.004 ± 0.028	2.081 ± 0.036	1.924 ± 0.043
Case 4	2.453 ± 0.004	2.829 ± 0.078	2.650 ± 0.012
Case 5	1.898 ± 0.054	3.448 ± 0.043	2.731 ± 0.028

Table 5b. Minimum Registration Error Using Exhaustive Search for Validating 3 Parameter Optimization

3	Left (mm)	Right (mm)	Whole (mm)
Case 1	1.386 ± 0.027	1.102 ± 0.054	1.186 ± 0.011
Case 2	1.325 ± 0.004	1.303 ± 0.007	1.287 ± 0.024
Case 3	1.791 ± 0.033	2.086 ± 0.027	1.923 ± 0.012
Case 4	2.454 ± 0.041	2.824 ± 0.067	2.654 ± 0.004
Case 5	1.870 ± 0.026	3.704 ± 0.016	2.525 ± 0.059

5.2 Convergence Study

While the theoretical convergence properties of FSA have been shown in literature [36, 37], we focus here on the experimental FSA-AMC convergence behavior as pertaining to its specific application of parameter optimization for 4D CT image registration. To evaluate the convergence behavior of FSA-AMC, the 2-parameter optimization was performed using the array of objective function values based on the smoothness factor and the number of solver iterations. Cost values for parameters that lied within the grid were interpolated using a linear interpolation technique. We performed FSA-AMC for each of the DIR-LAB cases with initial smoothness factor and solver iteration values farthest away from the found optimum value and without performing any initial uniform random sampling. In Fig 6, the achieved registration error for each specified number of iterations are plotted as the worst-case convergence behavior for FSA-AMC. The result shows that for all five cases, convergence was reached within 100 iterations.

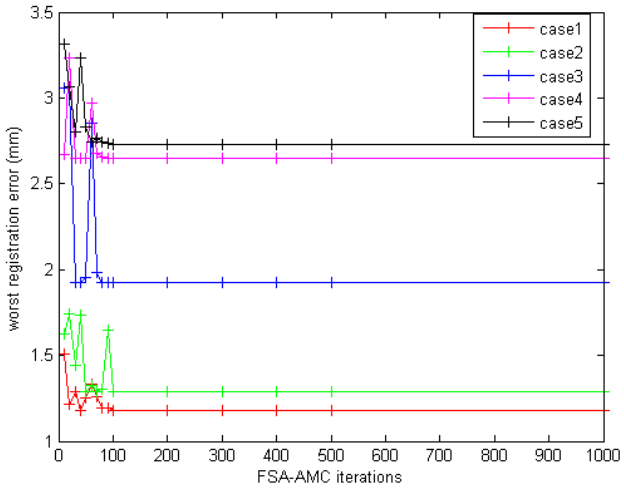

Figure 6. The worst case convergence of the registration error with number of iterations in worst-case scenarios for cases 1 through 5.

5.3 Computation Performance Study

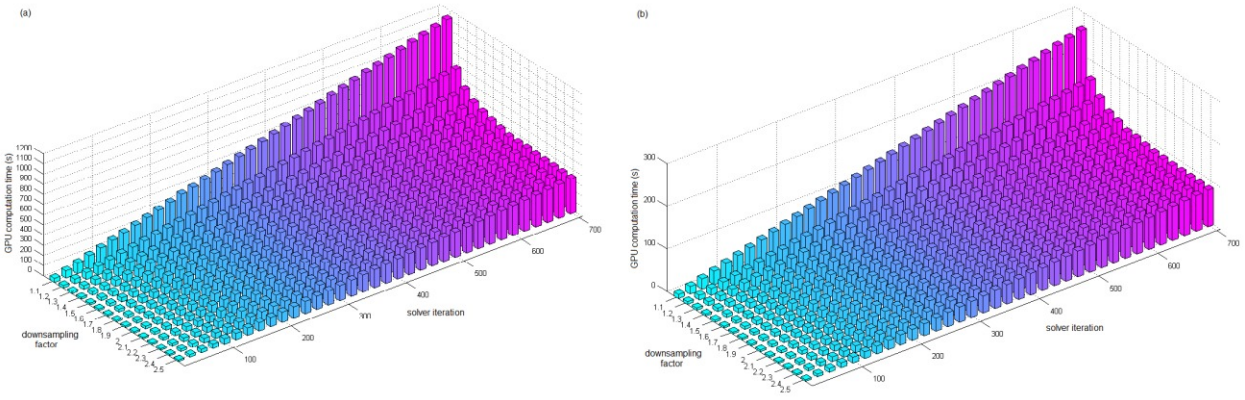

(a) (b)

Figure 7. GPU run time in dependence of the resolution levels and the solver iterations for a whole lung data (a) and separate lung data (b) on a NVIDIA GTX 680 GPU.

A GPU based dense optical flow registration algorithm (inner-most loop) was employed for our registration to achieve faster computation time [37]. The run-time however varied for variations in both the registration parameters. Computation time performances between the two methods, separate versus whole lung registration, in dependence of the solver iteration and the down sampling parameter, are shown in Fig 7. We employed a NVIDIA GTX 680 GPU for documenting the run-time. The data size for the whole lung was 256×256×104 while for the separate lung data, was 128×256×104. The maximum computation time for the whole lung registration was observed to be ~1100 seconds while the computation time for a separate lung registration was observed to be ~270 seconds. The median computation time ratio for maximum solver iteration and varying down sampling factor is approximately 4, whole lung registration versus separate. Such computation times demonstrate the fact that optimal registration parameters can be computed at acceptable computation times. Furthermore, with a large reduction in computation time and a negligible loss in registration accuracy, the approach of registering left and right lungs separately offers a significant computational advantage in further registration parameter analysis studies.

6 Discussion and Conclusion

In this paper, a novel approach to optimizing parameters for volumetric DIR using non-convex method is presented. The parameter optimization framework is examined using a dense optical-flow algorithm. The parameters subject to optimization were the smoothness factor, the number of optical-flow iteration, and the down-sampling factor in the multi-level registration scheme. The proposed joint parameter optimization was based on fast simulated annealing coupled with an adaptive Monte Carlo sampling method that efficiently searched through the entire parameter space. Application of the proposed method on both breathing model guided data and DIR-LAB data showed a wide variation in each of the optimized parameters across the studied cases. Registration error comparison in terms of mTRE between optimized parameter set and an arbitrary one varied widely, with an average difference of *0.39* mm and a maximum difference of *2.92* mm. These results demonstrated the impact on registration accuracy for a given image pair due to the optimized set of registration parameters and therefore showed the necessity for parameter optimization for DIR on a per subject basis. Optimization trials using 2 and 3 parameters showed that the obtained minimum mTRE, while differing only numerically in value, were found in significantly different parameter combinations. Thus, we in particular demonstrate explicitly the existence of multiple local minima using landmark-based objective function. The impact of multiple local minima may vary between the studied subject and the type of objective function. In addition, parametric optimization for single lung registrations shows widely different parameter combinations compared to

those of the whole lung registrations. Rigorous statistical analysis confirms the accuracy of such an approach to be equivalent to that obtained from the conventional whole lung registrations. Its significant reduction in computation time is an attractive feature for future lung registration studies.

Validation results showed that the optimal parameters and the estimated global minimum mTRE values obtained using the proposed method were in very good agreement with the results obtained independently using an exhaustive search approach. Moreover, we showed that the proposed method was highly efficient in demonstrating convergence to optimal parameters in worst-case scenarios. Albeit the optimization framework was demonstrated here for a multi-resolution optical flow algorithm for optimizing a total of three parameters, the proposed method is versatile and can be easily adopted in other registration methods with larger number of input parameters for benchmarking their optimum performance. Alternatively, the proposed method can serve as a comparative platform, where the variants of each of the internal registration modules, such as the transformation model, the optimization method, as well as the similarity measure can be systematically cross-examined with respect to their accuracy and performance.

Two key limitations of the FSA-AMC algorithm restrict it from being fully employed in a clinical setting are the computational complexity and its reliance on a landmark based objective function in the FSA loop. With respect to the former, future work will involve an exploration of the algorithmic performance dependence on the underlying cost function topography. The computational complexity of performing such parameter optimization analyses will be addressed using scalable high performance computing systems in order to efficiently perform a larger number of FSA-AMC iterations. To this end, statistical projection techniques will be investigated to optimally increase the number of iterations (outer loop) that can be done in a parallelized manner. Such an approach will reduce the computational time of the iterations (outer loop) significantly, and enable the algorithm to be computationally feasible in a clinical setting. In addition, training datasets will also be investigated for reducing the number of iterations (outer loop). Model-guided training dataset will an effective approach to generate pre-conditioners for each of the registration parameters.

As for the latter issue, the parameter optimization strategy discussed in this paper relies on the ground-truth data availability. Such ground-truth data will not be available in a clinical setting for all the 4DCT datasets. Future work will focus on re-defining the cost function using an image-based metric instead of a landmark-based metric in order to facilitate such analysis for clinical purposes. On this front, statistical metric and feature-based registration metrics will be employed. Model-guided training datasets with known ground-truth will be employed to quantitatively establish the image-based metric that provides the optimal registration accuracy. Lastly, while the proposed method is applied to optical-flow image registration in this paper, its utility is general and can find applications to other registration algorithms as well.

7 ACKNOWLEDGMENT

The authors would like to thank the National Science Foundation (#1200579) and Varian Inc for supporting this paper.

REFERENCES

[1] K. K. Brock and D. R. A. C, "Results of a Multi-Institution Deformable Registration Accuracy Study (Midras)," *International Journal of Radiation Oncology Biology Physics*, vol. 76, pp. 583-596, Feb 1 2010.

[2] K. Murphy, *et al.*, "Evaluation of Registration Methods on Thoracic CT: The EMPIRE10 Challenge," *Ieee Transactions on Medical Imaging*, vol. 30, pp. 1901-1920, Nov 2011.

[3] D. Sarrut, *et al.*, "Simulation of four-dimensional CT images from deformable registration between inhale and exhale breath-hold CT scans," *Medical Physics*, vol. 33, pp. 605-617, Mar 2006.
[4] D. A. Low, *et al.*, "A novel CT acquisition and analysis technique for breathing motion modeling," *Physics in Medicine and Biology*, vol. 58, pp. L31-L36, Jun 7 2013.
[5] J. Ehrhardt, *et al.*, "Statistical Modeling of 4D Respiratory Lung Motion Using Diffeomorphic Image Registration," *Ieee Transactions on Medical Imaging*, vol. 30, pp. 251-265, Feb 2011.
[6] R. Castillo, *et al.*, "A framework for evaluation of deformable image registration spatial accuracy using large landmark point sets," *Physics in Medicine and Biology*, vol. 54, pp. 1849-1870, Apr 7 2009.
[7] X. Gu, *et al.*, "Implementation and evaluation of various demons deformable image registration algorithms on a GPU," *Physics in Medicine and Biology*, vol. 55, pp. 207-19, Jan 7 2010.
[8] D. Sarrut, *et al.*, "A comparison framework for breathing motion estimation methods from 4-d imaging," *Ieee Transactions on Medical Imaging*, vol. 26, pp. 1636-1648, Dec 2007.
[9] N. Kadoya, *et al.*, "Evaluation of various deformable image registration algorithms for thoracic images," *Journal of radiation research*, 2013.
[10] E. Castillo, *et al.*, "Least median of squares filtering of locally optimal point matches for compressible flow image registration," *Physics in Medicine and Biology*, vol. 57, pp. 4827-4843, Aug 7 2012.
[11] V. Boldea, *et al.*, "4D-CT lung motion estimation with deformable registration: Quantification of motion nonlinearity and hysteresis," *Medical Physics*, vol. 35, pp. 1008-1018, Mar 2008.
[12] B. K. P. Horn and B. G. Schunck, "Determining Optical-Flow," *Artificial Intelligence*, vol. 17, pp. 185-203, 1981.
[13] B. D. D. S. Karsten Ostergaard Noe, Ulrik Vindelev Elstrom, Kari Tanderup, and Thomas Sangild Sorensen, "Acceleration and validation of optical flow based deformable registration for image-guided radiotherapy," *Acta Oncologica*, vol. 47, pp. 1286-1293, 2008/01/01 2008.
[14] M. Urschler, *et al.*, "Robust optical flow based deformable registration of thoracic CT images," *Medical Image Analysis for the Clinic: A Grand Challenge*, pp. 195-204, 2010.
[15] M. P. Heinrich, *et al.*, "Discontinuity preserving regularisation for variational optical-flow registration using the modified Lp norm," in *Medical Image Analysis for the Clinic-A Grand Challenge, Workshop MICCAI*, 2010, pp. 185-194.
[16] T. Guerrero, *et al.*, "Intrathoracic tumour motion estimation from CT imaging using the 3D optical flow method," *Physics in Medicine and Biology*, vol. 49, pp. 4147-4161, Sep 7 2004.
[17] S. S. Samant, *et al.*, "High performance computing for deformable image registration: Towards a new paradigm in adaptive radiotherapy," *Medical Physics*, vol. 35, pp. 3546-3553, Aug 2008.
[18] R. Kashani, *et al.*, "Objective assessment of deformable image registration in radiotherapy: A multi-institution study," *Medical Physics*, vol. 35, pp. 5944-5953, Dec 2008.
[19] B. Fischer and J. Modersitzki, "Ill-posed medicine - an introduction to image registration," *Inverse Problems*, vol. 24, Jun 2008.
[20] J. Rühaak, *et al.*, "Highly accurate fast lung CT registration," in *SPIE Medical Imaging*, 2013, pp. 86690Y-86690Y-9.
[21] M. P. Heinrich, *et al.*, "MRF-Based Deformable Registration and Ventilation Estimation of Lung CT," *Ieee Transactions on Medical Imaging*, vol. 32, pp. 1239-1248, Jul 2013.
[22] A. Schmidt-Richberg, *et al.*, "Landmark-driven Parameter Optimization for non-linear Image Registration," in *Proc. of SPIE Vol*, 2011, pp. 79620T-1.
[23] V. A. Morozov, *et al.*, *Methods for solving incorrectly posed problems*: Springer, 1984.
[24] D. L. Phillips, "A technique for the numerical solution of certain integral equations of the first kind," *Journal of the ACM (JACM)*, vol. 9, pp. 84-97, 1962.
[25] S. Lu and S. V. Pereverzev, "Multi-parameter regularization and its numerical realization," *Numerische Mathematik*, vol. 118, pp. 1-31, May 2011.
[26] P. Craven and G. Wahba, "Smoothing Noisy Data with Spline Functions - Estimating the Correct Degree of Smoothing by the Method of Generalized Cross-Validation," *Numerische Mathematik*, vol. 31, pp. 377-403, 1979.
[27] G. Wahba, *Spline models for observational data* vol. 59: Siam, 1990.
[28] P. C. Hansen, "Analysis of Discrete Ill-Posed Problems by Means of the L-Curve," *Siam Review*, vol. 34, pp. 561-580, Dec 1992.
[29] P. C. Hansen and D. P. Oleary, "The Use of the L-Curve in the Regularization of Discrete Iii-Posed Problems," *SIAM Journal on Scientific Computing*, vol. 14, pp. 1487-1503, Nov 1993.

[30] G. H. Golub and C. F. Van Loan, "Matrix computations. 1996," *Johns Hopkins University, Press, Baltimore, MD, USA*, pp. 374-426, 1996.
[31] C. R. Vogel, "Non-convergence of the L-curve regularization parameter selection method," *Inverse Problems*, vol. 12, pp. 535-547, Aug 1996.
[32] S. Kirkpatrick, *et al.*, "Optimization by Simulated Annealing," *Science*, vol. 220, pp. 671-680, 1983.
[33] H. Szu and R. Hartley, "Fast Simulated Annealing," *Physics Letters A*, vol. 122, pp. 157-162, Jun 8 1987.
[34] N. Metropolis, *et al.*, "Equation of State Calculations by Fast Computing Machines," *Journal of Chemical Physics*, vol. 21, pp. 1087-1092, 1953.
[35] D. Thomas, *et al.*, "A Novel Fast Helical 4D-CT Acquisition Technique to Generate Low-Noise Sorting Artifact–Free Images at User-Selected Breathing Phases," *International Journal of Radiation Oncology*Biology*Physics*.
[36] A. Dekkers and E. Aarts, "Global Optimization and Simulated Annealing," *Mathematical Programming*, vol. 50, pp. 367-393, Jun 1991.
[37] D. Mitra, *et al.*, "Convergence and finite-time behavior of simulated annealing," in *Decision and Control, 1985 24th IEEE Conference on*, 1985, pp. 761-767.